

# Improving Automated Hemorrhage Detection in Sparse-view Computed Tomography via Deep Convolutional Neural Network based Artifact Reduction

Johannes Thalhammer<sup>1-4</sup>, Manuel Schultheiß<sup>1-3</sup>, Tina Dorosti<sup>1-3</sup>, Tobias Lasser<sup>2,5</sup>, Franz Pfeiffer<sup>1-4</sup>, Daniela Pfeiffer<sup>1-4</sup>, Florian Schaff<sup>1-2</sup>

**Summary statement:** By post-processing sparse-view cranial computed tomography scans with neural networks, the number of views can be reduced from 4096 to 512 with minimal impact on automated hemorrhage detection, and to 256 with only a slight performance decrease.

## Key points:

1. Reducing artifacts in sparse-view cranial CTs improved automated hemorrhage detection across all investigated subtypes.
2. A comparison of a convolutional neural network (CNN) to a total-variation-based approach for artifact reduction in sparse-view cranial CTs showed that the CNN-based approach achieved superior performance regarding artifact reduction, image quality parameters, and subsequent automated hemorrhage diagnosis.

**Abbreviations:** Area Under the Receiver Operator Characteristic Curve (AUC-ROC), Receiver Operator Characteristic Curve (ROC), Confidence Interval (CI), Convolutional Neural Network (CNN), Computed Tomography (CT), Filtered Back Projection (FBP), Intracranial Hemorrhage (ICH), Mean Squared Error (MSE), Peak Signal-to-noise Ratio (PSNR), Structural Similarity Index (SSIM), Total Variation (TV)

**Keywords:** Artifact reduction, computed tomography (CT), deep learning, hemorrhage detection, sparse-view CT, U-Net

<sup>1</sup> Chair of Biomedical Physics, Department of Physics, School of Natural Sciences, Technical University of Munich, 85748 Garching, Germany

<sup>2</sup> Munich Institute of Biomedical Engineering, Technical University of Munich, 85748 Garching, Germany

<sup>3</sup> Department of Diagnostic and Interventional Radiology, School of Medicine, Klinikum rechts der Isar, Technical University of Munich, 81675 Munich, Germany

<sup>4</sup> Institute for Advanced Study, Technical University of Munich, 85748 Garching, Germany

<sup>5</sup> Computational Imaging and Inverse Problems, Department of Computer Science, School of Computation, Information, and Technology, Technical University of Munich, 85748 Garching, Germany

## Funding:

Funded by the Federal Ministry of Education and Research (BMBF) and the Free State of Bavaria under the Excellence Strategy of the Federal Government and the Länder, the German Research Foundation (GRK2274), as well as by the Technical University of Munich–Institute for Advanced Study.

## Abstract

**Purpose:** Sparse-view computed tomography (CT) is an effective way to reduce dose by lowering the total number of views acquired, albeit at the expense of image quality, which, in turn, can impact the ability to detect diseases. We explore deep learning-based artifact reduction in sparse-view cranial CT scans and its impact on automated hemorrhage detection.

**Methods:** We trained a U-Net for artefact reduction on simulated sparse-view cranial CT scans from 3000 patients obtained from a public dataset and reconstructed with varying levels of sub-sampling. Additionally, we trained a convolutional neural network on fully sampled CT data from 17,545 patients for automated hemorrhage detection. We evaluated the classification performance using the area under the receiver operator characteristic curves (AUC-ROCs) with corresponding 95% confidence intervals (CIs) and the DeLong test, along with confusion matrices. The performance of the U-Net was compared to an analytical approach based on total variation (TV).

**Results:** The U-Net performed superior compared to unprocessed and TV-processed images with respect to image quality and automated hemorrhage diagnosis. With U-Net post-processing, the number of views can be reduced from 4096 (AUC-ROC: 0.974; 95% CI: 0.972-0.976) views to 512 views (0.973; 0.971-0.975) with minimal decrease in hemorrhage detection ( $P < .001$ ) and to 256 views (0.967; 0.964-0.969) with a slight performance decrease ( $P < .001$ ).

**Conclusion:** The results suggest that U-Net based artifact reduction substantially enhances automated hemorrhage detection in sparse-view cranial CTs. Our findings highlight that appropriate post-processing is crucial for optimal image quality and diagnostic accuracy while minimizing radiation dose.

## 1 Introduction

Intracranial hemorrhage (ICH) is a potentially life-threatening disease with a 30-day fatality rate of 40.4%, accounting for 10% to 30% of annual strokes [1][2]. Prompt and accurate diagnosis is vital for optimal treatment, typically achieved through cranial Computed Tomography (CT) scans [3]. However, the increased use of medical CT scans, including cranial scans, raises concerns about radiation-related health risks [4] [5]. A routine head CT exposes patients to a median effective dose of 2 mSv, similar to natural radiation accumulated per year. Not only does this affect the brain, but also nearby areas, for example the sensitive eye lenses [5] [6].

Besides lowering the X-ray tube current, sparse-view CT is a promising approach to reduce dose by decreasing the number of views. However, this reduction causes artifacts in the filtered back projection (FBP) reconstructed images. To restore image quality for accurate diagnosis, suitable processing methods are needed. In the past, compressed sensing (CS) and iterative reconstruction approaches have been widely investigated, which generally minimize a CS-based regularization term as well as a data-fidelity term that ensures data consistency. These approaches have been proven to yield good results in terms of reducing image noise and artifacts. However, they are also computationally demanding due to the repeated update steps during iterative optimization. Additionally, these methods require parameter optimization and can alter image texture [7] [8] [9]. Recently, machine learning approaches using deep neural networks have gathered vast scientific attention. In the context of artefact reduction in sparse-view CT, it has been shown that convolutional neural networks are able to achieve excellent results with comparably low computational effort during inference [10] [11] [12]. Approaches that combine deep learning and iterative techniques for sparse-view artifact reduction can also be found in the literature [13] [14].

In parallel, extensive research has been conducted on the application of deep learning techniques for automated detection and classification of pathological features in CT images and many systems are already FDA-approved and CE-certified [15] [16] [17]. These algorithms are usually trained on standard-dose data however, limiting their use on dose reduced, e.g., sparse-view data, as additional noise and artifacts are expected to negatively impact the reliability of such systems.

Therefore, in this study, our aim is twofold. Firstly, we aim to explore the potential benefits of deep learning-based artifact reduction in sparse-view cranial CTs. Secondly, we assess whether this approach can enhance the performance of automated hemorrhage detection.

## Methods

The code is available at: <https://github.com/J-3TO/Sparse-View-Cranial-CT-Reconstruction>.

### 2.1 Network Architectures

Figure 2 depicts the used U-Net architecture for artefact reduction with an additional skip connection between network input and output [18]. Pooling is performed by strided convolutions with stride (2, 2), followed by a 1x1 convolution. Unpooling is implemented with transposed strided convolutions, again with stride (2, 2) which was adapted from Guo et al. [19]. If not stated otherwise, each block of feature channels is connected to its previous one by a 3x3 convolution. The model was initialized with random weights. For hemorrhage classification, the EfficientNetB2 implemented in Keras (version 2.0.4) was used, initialized with ImageNet pretrained weights [20] [21].

### 2.2 Datasets

This retrospective study used the RSNA 2019 Brain CT Hemorrhage Challenge dataset [22], with each CT image annotated for hemorrhage presence and subtype (subarachnoid, intraventricular, subdural, epidural, and intraparenchymal) [22] [23]. The dataset consists of CT scans from 18,938 different patients. After filtering out images with either not 512x512 pixels or lead to some different error

during data generation, 18,545 patients remained. Data from 1,000 patients were randomly selected for testing and excluded from all further training.

For U-Net training, 3,000 patients were randomly selected from the remaining dataset. 2400 patients (80%) served as training data, and 600 patients (20%) as validation data. The pixel intensities in the DICOM format usually range from 0 to 40995 (12-bit numbers). To create sparse-view CTs, the data was normalized to range [0, 1] by division by 4095. Sinograms with 4096 views were created under parallel beam geometry from the CT dataset using the Astra Toolbox (version 2.1.0) [24]. Ground truth images were reconstructed from 4096 views using FBP. Six sparse-view subsets were generated using FBP with only 64, 128, 256, 512, 1024 and 2048 views, respectively.

Due to overfitting concerns, the remaining dataset except the test split was used for training the EfficientNetB2 (17,545 patients). Individual images were scaled to Hounsfield Units (HUs) and clipped to the diagnostically relevant brain window [0-80] HU. To meet the requirements of the pre-trained ImageNet, images were rescaled to [0-255], resized to 260x260 pixels by bilinear resizing and transformed to three channel images by concatenating three neighboring CT images [25].

Figure 1a) depicts the data selection process and b) the distribution of the labelled hemorrhage subtypes.

For external validation, 10,000 images were randomly chosen from the CQ500 dataset (mean age 48.13 (7-95), 36.25% female) derived from the Centre for Advanced Research in Imaging, Neurosciences and Genomics (CARING), New Delhi, India [26]. These images were pre-processed in the same manner as the RSNA dataset.

### 2.3 Training

The U-Net was trained separately for each sparse-view subset, using sparse-view images as input and full-view images as ground truth. It was trained with mean squared error loss for 75 epochs with a mini-batchsize of 32. Randomly selected 256x256 patches from the images were rotated by 0°, 90°, 180°, or 270°. The learning rate was  $lr=10^{-4}/(\text{epoch}+1)$ . The EfficientNetB2 was trained with 5-fold cross-validation and binary cross-entropy loss with a mini-batchsize of 32 for 15 epochs. The learning rate followed a cosine annealing schedule with warm restarts after epoch one, three, and seven with an initial learning rate of  $5 \cdot 10^{-4}$  and minimal learning rate of  $10^{-5}$ . The model with the lowest validation loss was selected for each split. The predictions for each image were averaged across the five models.

### 2.4 Total Variation

In this work, we used the isotropic total variation (TV) method by Chambolle for artefact reduction (scikit-image version 0.19.3) [27] [28]. The optimal weight for each sparse subset was determined by randomly sampling 1000 images from the U-Net training set and iterating through weights ranging from 0.001 to 1.000 in 0.001 increments. We identified a global maximum within this weight range for each subset, suggesting the range was reasonable. The weights that yielded the best score on the structural similarity index measure (SSIM) were selected to calculate the metrics on the test set [29].

### 2.5 Saliency Maps

The saliency maps were obtained by computing the gradient of the class score with respect to the input image, as described in [30].

### 2.6 Statistical Analysis

Image quality of the different post-processing methods were compared using SSIMs and peak signal-to-noise-ratios (PSNRs). 95% CIs were calculated and two-sided paired t-tests were performed to examine significant differences using SciPy (version 1.4.1). To quantify hemorrhage classification performance, empirical area under the receiver operator characteristic curves (AUC-ROCs) including 95% CIs were estimated as described by DeLong et al. Statistical differences in AUC-ROCs between sparse-view and full-view, as well as between different post-processing methods, were evaluated

using the DeLong two-sided test [31] [32]. Confusion matrices were generated with Scikit-learn (version 1.1.3), the discrimination thresholds were selected for each subset to maximize the geometric mean of the true positive and the true negative rate [33].

## 3 Results

### 3.1 Artifact Reduction

Figure 3 shows a CT image from the test set, reconstructed with varying number of views. The top row displays raw images, and the bottom row demonstrates artifact reduction by the U-Net. The labelled intraparenchymal and intraventricular hemorrhages are shown in detail in the zoomed-in extracts. All images are displayed in the brain window. In a), the full-view (4096 views) shows a clearly visible intraparenchymal hemorrhage (cyan arrow). The intraventricular subtype (orange arrow) is also discernible, although it is more challenging to detect. In b), the image quality starts to deteriorate, and artifacts appear. Nevertheless, the hemorrhages can still be identified. In c) streak artifacts become pronounced, making it challenging to distinguish small features. Although the intraparenchymal subtype is still discernible, the intraventricular subtype is barely recognizable. Images d) and e) show severe streak artifacts and distortion of the brain tissue. The hemorrhages are no longer recognizable. In images f) - i) the U-Net predictions of the sparse-view images are depicted, revealing a clear reduction in streak artifacts compared to the respective input images b) - e). With increasingly sparse-sampled input, the prediction also tends to become smoother, i.e., sharp image features are not retained. However, image quality of the sparse-view CTs still improves, and the similarity between predictions and full-view images increases. The contours of the hemorrhage can be recognized down to and including 128-view (h) and 256-view (g) predictions for intraparenchymal and intraventricular subtypes, respectively.

### 3.2 Comparison with Total Variation (TV)

For comparison, we also implemented TV-based artefact reduction, which is commonly used for undersampling problems [34] [35]. Figure 4 displays results of an image labeled "healthy" from the test set processed in various ways. SSIM and PSNR values in the figure were calculated based on the 4096-view image. Images a) - f) show the image reconstructed from 2048, 1024, 512, 256, 128, and 64 views without any post-processing, respectively. While in (a) no artifacts are visible, the image quality deteriorates if the number of views is further reduced, with only the skull shape discriminable in the 64-view reconstruction (e). In g) - m), the respective predictions by the U-Net of the sparse-view CTs in the upper row are shown. Consistent with figure 3, the U-Net reduces the artifacts considerably. We once again note that the resulting images are increasingly smoothed as the number of views decreases. In images n) - s) the results of TV post-processing are depicted, which can reduce the artifacts well down to 256 views sparse sampling. However, the results for 128- and 64-sparse view data are inferior compared to the results from U-Net post-processing.

Table 1 presents the mean SSIM and PSNR values of the reconstructed images calculated on the RSNA test set and the CQ500 dataset, with individual values calculated in reference to the 4096-view images. Both, U-Net and the TV post-processing quantitatively increased the SSIM by reducing streak artifacts compared to raw FBP reconstructions. This aligns with visual results in figures 3 and 4. U-Net post processing also enhanced PSNR values, whereas TV-processing resulted in decreased PSNR values for specific subsets, specifically for the RSNA test split down to including 512-views and for the 2048-view image of the CQ500 dataset, when compared to the respective raw FBP images. The PSNR values of the remaining subsets improved after TV-processing. Direct comparison revealed U-Net's stronger performance in all cases, with statistically significant differences between post-processing for each subset ( $P < .001$ ).

### 3.3 Detection of Hemorrhage Subtypes

Finally, we evaluate the impact of artifact reduction on automated hemorrhage detection by examining the outcomes of the EfficientNetB2 hemorrhage classification network. In figure 5 the AUC-ROC values for the raw images (blue) and the images post-processed by either TV (green) or the U-Net (orange) are shown for varying levels of subsampling. In a) the AUC-ROC values of the "any" class are depicted, indicating whether any kind of hemorrhage is present in the CT image. Subfigures b) - f) show the AUC-ROC plots of the classified subtypes: subdural, subarachnoid, intraparenchymal, intraventricular, and epidural. Overall, classification performance declines as the number of views used for the reconstruction decreases. For raw FBP reconstructions, the 2048-view images yield nearly identical AUC-ROC values as the full-view images ( $P > .01$ ). When reducing the number of views to 1024, there is a slight decrease in performance ( $P < .001$ ), which further drops with fewer views. In TV post-processed images, the AUC-ROC values slightly decrease down to 512-views ( $P < .001$ ) and decline substantially for fewer views. With the U-Net, the number of views can be reduced from 4096 views down to 512 views with a minimal decrease ( $P < .001$ ) in classification performance, and down to 256 views with only a slight performance decrease. Below 256 views, a noticeable decline is visible. In all the cases reconstructed with 1024 views or fewer, the AUC-ROC values obtained from U-Net post-processed images surpass those of TV-processed and raw sparse-view images significantly ( $P < .001$ ). Notably, the detection of epidural hemorrhages is generally poorer compared to other subtypes. Table 2 shows the confusion matrices for the 'any' class of CT images reconstructed with varying number of views, without post-processing (FBP), and with either TV or U-Net post-processing. The decrease in classification performance and the impact of post-processing agree with the results in figure 5. The ROC curves used to calculate the ROC-AUCs, the individual ROC-AUCs, and the confusion matrices for all classes can be found in the supplementary materials.

### 3.4 Saliency Maps

Figure 6 shows the saliency maps for the images of figure 3 with regards to the 'any' class. The rectangles are positioned identically to those in figure 3, indicating the location of the hemorrhages. For images reconstructed down to and including 256-view sparse-sampling (subfigures a) - c)), the network primarily focused on the area of the intraparenchymal hemorrhage for its prediction. However, for reconstructions with fewer views (subfigures d) and f)), such a focused area is no longer discernible. Conversely, for the U-Net post-processed images (subfigures f) - i)) all the saliency maps exhibit a clear emphasis on the subarachnoid hemorrhage area.

## 4 Discussion

In this work we investigated convolutional neural network-based artifact reduction in sparse-view cranial CTs and the subsequent impact on automated hemorrhage detection and classification. We demonstrated that a deep convolutional neural network, specifically a U-Net architecture, leads to substantial improvements in the visual quality of sparse-view cranial CTs. Evaluation using the PSNR and SSIM metrics confirmed quantitatively the enhanced image quality achieved by the network. Furthermore, we trained a hemorrhage detection and classification network on full-view CT images and applied it to sparse-view images with and without post-processing by the U-Net. The results showed that the U-Net enabled a reduction in views from 4096 to 512 with minimal impact on classification performance, and to 256 views with only a slight performance decrease. Additionally, we compared the results of the U-Net with an analytical approach based on TV. The U-Net was found to perform superior to TV post-processing with respect to image quality parameters and automated hemorrhage diagnosis.

The artifact reduction performance of our network was comparable to similar methods. Examples are the works by Han et al., who proposed a U-Net with an additional skip connection from the input to the final output, or Jin et al., who extended the U-Net architecture to satisfy the frame condition [10] [11]. The success of these architectures, including our U-Net, can be attributed to their multi-

resolution feature. The exponentially large receptive field due to the pooling and unpooling layers makes it possible to handle streak artifacts that occur in sparse-view CT and typically spread over a large portion of the image.

The U-Net demonstrated robustness by substantially improving image quality across all investigated levels of subsampling on both the RSNA dataset and the external CQ500 dataset. This was evidenced by the calculated PSNR and SSIM values. The TV approach was also able to significantly improve the SSIM values of the sparse-view data. Interestingly, no clear trend in the PSNR values could be identified for TV processing. This is most likely because the weights for the TV method were set to optimize the SSIM, rather than PSNR, as described in section 2.4. The results of automated hemorrhage detection further validated the importance of artifact reduction, with substantial improvements observed in AUC-ROC values and confusion matrices. Saliency maps provided additional support to these findings by revealing that pronounced artifacts in sparse-view images disrupted the classification process, leading to increased false positives and false negatives. By reducing these artifacts through post-processing, these effects can be mitigated, and the classification performance can be maintained, without the need for specific training on sub-sampled data.

It is important to acknowledge some limitations of this study. The sparse-view data used in our study was retrospectively generated under simplified conditions from CT volumes, which may not fully capture the complexity of real-world scenarios. Additionally, the training dataset had imbalances in terms of negative cases and not all hemorrhage subtypes were represented equally. This might explain the relatively poor performance in classifying the epidural subtype compared to the other subtypes. Furthermore, analyzing the patient demographics across data splits was not possible due to the unavailability of such information in the RSNA dataset.

Our findings highlight the importance of employing appropriate post-processing techniques to achieve optimal image quality and diagnostic accuracy while minimizing radiation dose. Furthermore, our study demonstrates that leveraging deep learning methods for artifact reduction can lead to significant improvements in the classification performance of sparse-view cranial CTs. This has promising implications for rapid automated hemorrhage classification on sparse-view cranial CT data to assist radiologists in routine clinical practice.

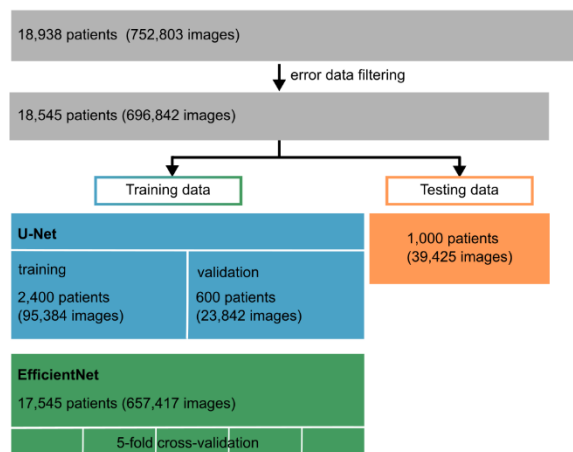


## References

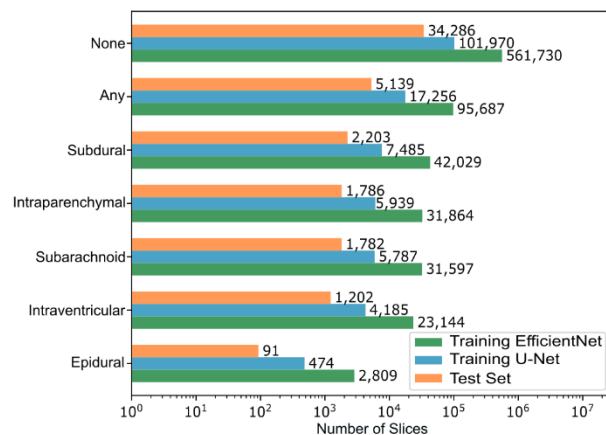
- [1] Charlotte JJ van Asch et al. "Incidence, case fatality, and functional outcome of intracerebral haemorrhage over time, according to age, sex, and ethnic origin: a systematic review and meta-analysis". In: *The Lancet Neurology* 9.2 (Feb. 2010), pp. 167–176. issn: 14744422. doi: 10.1016/S1474-4422(09)70340-0. url: <https://linkinghub.elsevier.com/retrieve/pii/S1474442209703400>.
- [2] Valery L Feigin et al. "Worldwide stroke incidence and early case fatality reported in 56 population-based studies: a systematic review". In: *The Lancet Neurology* 8.4 (Apr. 2009), pp. 355–369. issn: 14744422. doi: 10.1016/S1474-4422(09)70025-0. url: <https://linkinghub.elsevier.com/retrieve/pii/S1474442209700250>.
- [3] Stuart Currie et al. "Imaging assessment of traumatic brain injury". In: *Postgraduate Medical Journal* 92.1083 (Jan. 2016), pp. 41–50. issn: 0032-5473. doi: 10.1136/postgradmedj-2014-133211. url: <https://pmj.bmj.com/lookup/doi/10.1136/postgradmedj-2014-133211>.
- [4] David J. Brenner and Eric J. Hall. "Computed Tomography — An Increasing Source of Radiation Exposure". In: *New England Journal of Medicine* 357.22 (2007). issn: 0028-4793. doi: 10.1056/nejmra072149.
- [5] Rebecca Smith-Bindman et al. "Radiation dose associated with common computed tomography examinations and the associated lifetime attributable risk of cancer". In: *Archives of Internal Medicine* 169.22 (2009). issn: 00039926. doi: 10.1001/archinternmed.2009.427.
- [6] Rebekah Poon and Mohamed K Badawy. "Radiation dose and risk to the lens of the eye during CT examinations of the brain". In: *Journal of Medical Imaging and Radiation Oncology* 63.6 (Dec. 2019), pp. 786–794. issn: 1754-9477. doi: 10.1111/1754-9485.12950. url: <https://onlinelibrary.wiley.com/doi/10.1111/1754-9485.12950>.
- [7] Zhanli Hu et al. "An improved statistical iterative algorithm for sparse-view and limited-angle CT image reconstruction". In: *Scientific Reports* 7.1 (Sept. 2017), p. 10747. issn: 2045-2322. doi: 10.1038/s41598-017-11222-z. url: <https://www.nature.com/articles/s41598-017-11222-z>.
- [8] Ludwig Ritschl et al. "Improved total variation-based CT image reconstruction applied to clinical data". In: *Physics in Medicine and Biology* 56.6 (Mar. 2011), pp. 1545–1561. issn: 0031-9155. doi: 10.1088/0031-9155/56/6/003. url: <https://iopscience.iop.org/article/10.1088/0031-9155/56/6/003>.
- [9] Pascal Th´eriault Lauzier and Guang-Hong Chen. "Characterization of statistical prior image constrained compressed sensing (PICCS): II. Application to dose reduction". In: *Medical Physics* 40.2 (Jan. 2013), p. 021902. issn: 00942405. doi: 10.1118/1.4773866. url: <http://doi.wiley.com/10.1118/1.4773866>.
- [10] Yoseob Han and Jong Chul Ye. "Framing U-Net via Deep Convolutional Framelets: Application to SparseView CT". In: *IEEE Transactions on Medical Imaging* 37.6 (2018). issn: 1558254X. doi: 10.1109/TMI.2018.2823768.
- [11] Kyong Hwan Jin et al. "Deep Convolutional Neural Network for Inverse Problems in Imaging". In: *IEEE Transactions on Image Processing* 26.9 (Sept. 2017), pp. 4509–4522. issn: 1057-7149. doi: 10.1109/TIP.2017.2713099. url: <http://ieeexplore.ieee.org/document/7949028/>.
- [12] Theodor Cheslorean-Boghiu et al. "WNet: A Data-Driven Dual-Domain Denoising Model for Sparse-View Computed Tomography With a Trainable Reconstruction Layer". In: *IEEE Transactions on Computational Imaging* 9 (2023). issn: 23339403. doi: 10.1109/TCI.2023.3240078.
- [13] Weiwen Wu et al. "DRONE: Dual-Domain Residual-based Optimization NETwork for Sparse-View CT Reconstruction". In: *IEEE Transactions on Medical Imaging* 40.11 (Nov. 2021), pp. 3002–3014. issn: 0278-0062. doi: 10.1109/TMI.2021.3078067. url: <https://ieeexplore.ieee.org/document/9424618/>.
- [14] Gaoyu Chen et al. "4D-AirNet: a temporally-resolved CBCT slice reconstruction method synergizing analytical and iterative method with deep learning". In: *Physics in Medicine & Biology* 65.17 (Sept. 2020), p. 175020. issn: 1361-6560. doi: 10.1088/1361-6560/ab9f60. url: <https://iopscience.iop.org/article/10.1088/1361-6560/ab9f60>.
- [15] Xiyue Wang et al. "A deep learning algorithm for automatic detection and classification of acute intracranial hemorrhages in head CT scans". In: *NeuroImage: Clinical* 32 (2021), p. 102785. issn: 22131582. doi: 10.1016/j.nicl.2021.102785. url: <https://linkinghub.elsevier.com/retrieve/pii/S2213158221002291>.
- [16] Artificial Intelligence and Machine Learning (AI/ML)-Enabled Medical Devices online: <https://www.fda.gov/medical-devices/software-medical-device-samd/artificial-intelligence-and-machine-learning-aiml-enabled-medical-devices> (accessed on 10 July 2023)



- [17] Brainscan.ai. Available online: <https://brainscan.ai/> (accessed on 10 July 2023)
- [18] Olaf Ronneberger, Philipp Fischer, and Thomas Brox. "U-net: Convolutional networks for biomedical image segmentation". In: *Lecture Notes in Computer Science (including subseries Lecture Notes in Artificial Intelligence and Lecture Notes in Bioinformatics)*. Vol. 9351. 2015. doi: 10.1007/978-3-319-24574-4\_28.
- [19] Shi Guo et al. "Toward convolutional blind denoising of real photographs". In: *Proceedings of the IEEE Computer Society Conference on Computer Vision and Pattern Recognition*. Vol. 2019-June. 2019. doi: 10.1109/CVPR.2019.00181. Page 12
- [20] Mingxing Tan and Quoc V. Le. "EfficientNet: Rethinking model scaling for convolutional neural networks". In: *36th International Conference on Machine Learning, ICML 2019*. Vol. 2019-June. 2019.
- [21] François Chollet. Keras. 2015. url: <https://github.com/fchollet/keras>.
- [22] RSNA Intracranial Hemorrhage Detection Challenge (2019). url: <https://www.rsna.org/education/ai-resources-and-training/ai-image-challenge/rsna-intracranial-hemorrhage-detectionchallenge-2019>.
- [23] Adam E. Flanders et al. "Construction of a Machine Learning Dataset through Collaboration: The RSNA 2019 Brain CT Hemorrhage Challenge". In: *Radiology: Artificial Intelligence* 2.3 (May 2020), e190211. issn: 2638-6100. doi: 10.1148/ryai.2020190211. url: <http://pubs.rsna.org/doi/10.1148/ryai.2020190211>.
- [24] W. J. Palenstijn, K. J. Batenburg, and J. Sijbers. "Performance improvements for iterative electron tomography reconstruction using graphics processing units (GPUs)". In: *Journal of Structural Biology* 176.2 (2011). issn: 10478477. doi: 10.1016/j.jsb.2011.07.017.
- [25] Martín Abadi et al. "Tensorflow: Large-scale machine learning on heterogeneous distributed systems. arXiv 2016". 2019.
- [26] Sasank Chilamkurthy et al. "Deep learning algorithms for detection of critical findings in head CT scans: a retrospective study". In: *The Lancet* 392.10162 (2018). issn: 1474547X. doi: 10.1016/S0140-6736(18)31645-3.
- [27] Antonin Chambolle. "An Algorithm for Total Variation Minimization and Applications". In: *Journal of Mathematical Imaging and Vision*. Vol. 20. 1-2. 2004. doi: 10.1023/B:JMIV.0000011321.19549.88.
- [28] Stéfan van der Walt et al. "scikit-image: image processing in Python". In: *PeerJ* 2.1 (June 2014), e453. issn: 2167-8359. doi: 10.7717/peerj.453. url: <https://peerj.com/articles/453>.
- [29] Z. Wang et al. "Image Quality Assessment: From Error Visibility to Structural Similarity". In: *IEEE Transactions on Image Processing* 13.4 (Apr. 2004), pp. 600–612. issn: 1057-7149. doi: 10.1109/TIP.2003.819861. url: <http://ieeexplore.ieee.org/document/1284395/>.
- [30] Karen Simonyan, Andrea Vedaldi, and Andrew Zisserman. "Deep inside convolutional networks: Visualising image classification models and saliency maps". In: *2nd International Conference on Learning Representations, ICLR 2014 - Workshop Track Proceedings*. 2014.
- [31] Elizabeth R. DeLong, David M. DeLong, and Daniel L. Clarke-Pearson. "Comparing the Areas under Two or More Correlated Receiver Operating Characteristic Curves: A Nonparametric Approach". In: *Biometrics* 44.3 (1988). issn: 0006341X. doi: 10.2307/2531595
- [32] Xu Sun and Weichao Xu. "Fast implementation of DeLong's algorithm for comparing the areas under correlated receiver operating characteristic curves". In: *IEEE Signal Processing Letters* 21.11 (2014). issn: 10709908. doi: 10.1109/LSP.2014.2337313.
- [33] Fabian Pedregosa et al. "Scikit-learn: Machine learning in Python". In: *Journal of Machine Learning Research* 12 (2011). issn: 15324435.
- [34] Emil Y Sidky and Xiaochuan Pan. "Image reconstruction in circular cone-beam computed tomography by constrained, total-variation minimization". In: *Physics in Medicine and Biology* 53.17 (Sept. 2008), pp. 4777–4807. issn: 0031-9155. doi: 10.1088/0031-9155/53/17/021. url: <https://iopscience.iop.org/article/10.1088/0031-9155/53/17/021>.
- [35] Yi Zhang et al. "Few-view image reconstruction with fractional-order total variation". In: *Journal of the Optical Society of America A* 31.5 (May 2014), p. 981. issn: 1084-7529. doi: 10.1364/JOSAA.31.000981. url: <https://opg.optica.org/abstract.cfm?URI=josaa-31-5-981>.



a) Data Selection



b) Distribution of hemorrhage cases

**Figure 1.** a) Flowchart of the data selection process. b) Distribution of the labeled hemorrhage subtypes in the used data split of the EfficientNetB2, the U-Net and the test set. Note the logarithmic scaling of the x-axis.

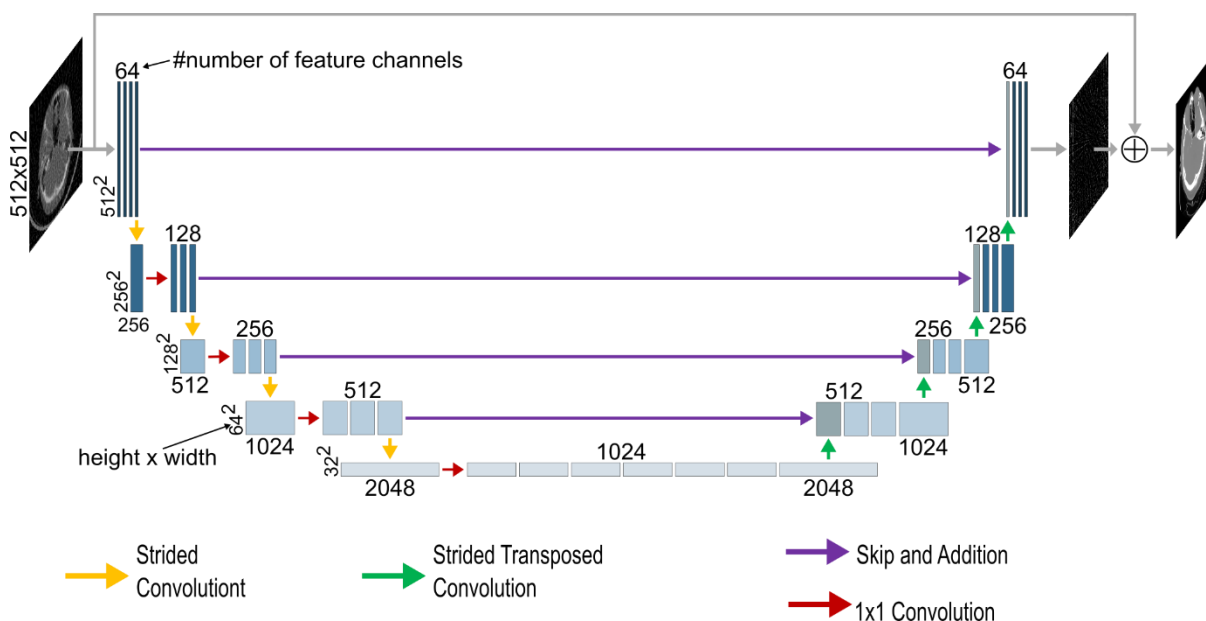


**Figure 2.** The architecture of the used U-Net for a 512x512 input. If not stated each block of feature channels is connected to the previous one by a 3x3 convolution.

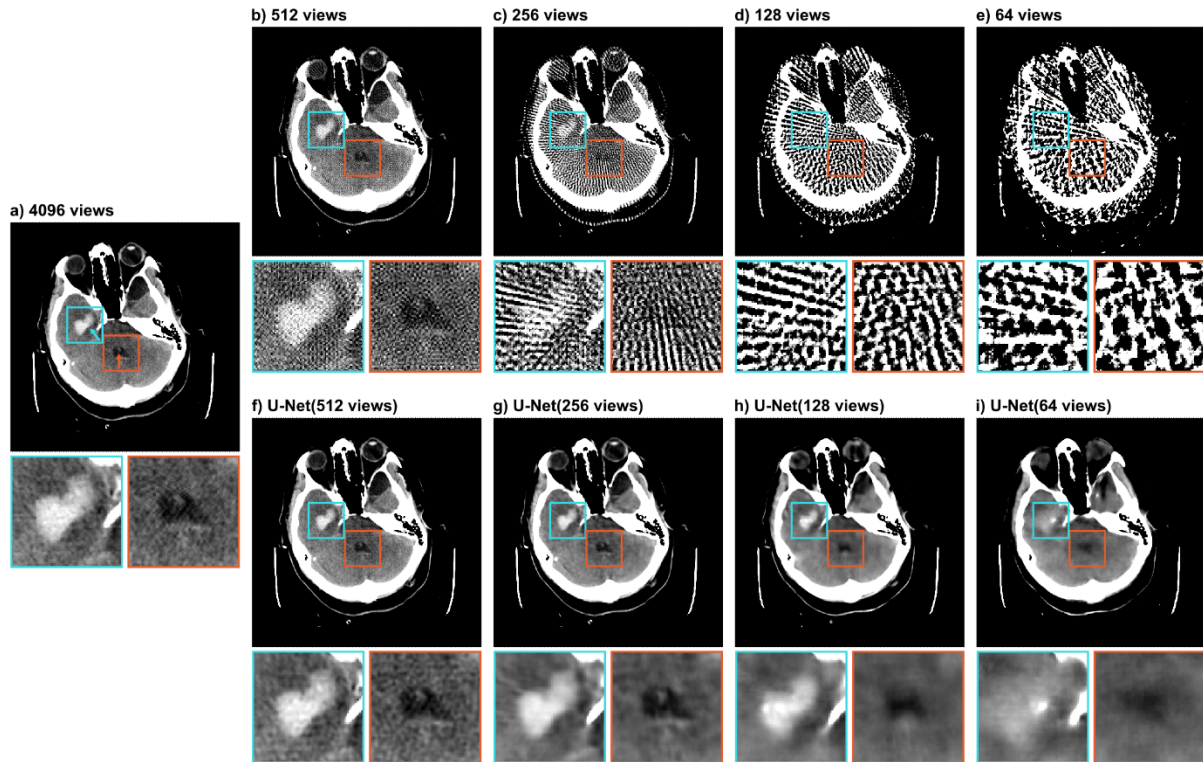


**Figure 3.** CT image (512x512 pixels) from the test set labeled with an intraparenchymal (cyan arrow) and an intraventricular (orange arrow) hemorrhage. Image a) shows the image reconstructed from 4096 views. Images b) - e) show the same image reconstructed from 512, 256, 128, and 64 views, respectively. Images f) - i) show the U-Net predictions of the corresponding sparse-view images in the upper row. All images are presented in the brain window ranging from 0 HU to 80 HU. Both inserts are 80x80 pixels.

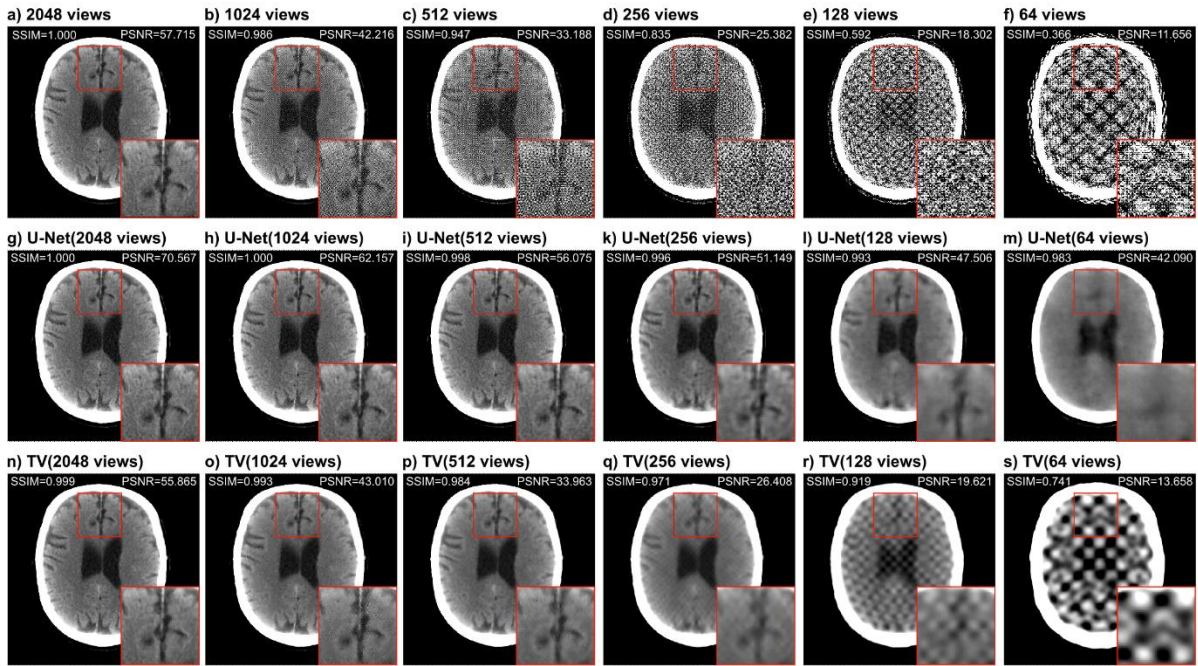


**Figure 4:** CT image (512x512 pixels) from the test set labeled as "healthy". Images a) - f) show the FBP reconstruction from 2048, 1024, 512, 256, 128, and 64 views, respectively. Images g) - m) show the U-Net predictions of the respective images in the upper row, and images n) - s) show the results of the total variation-based method. The presented structural similarity index measure (SSIM) and Peak signal-to-noise ratio (PSNR) values were calculated over the entire CT image scaled to [0- 1] from the full Hounsfield unit range [-1024-3071] HU. All images are presented in the brain window ranging from 0 HU to 80 HU. The insert is 100x100 pixels, the entire image is 512x512 pixels.

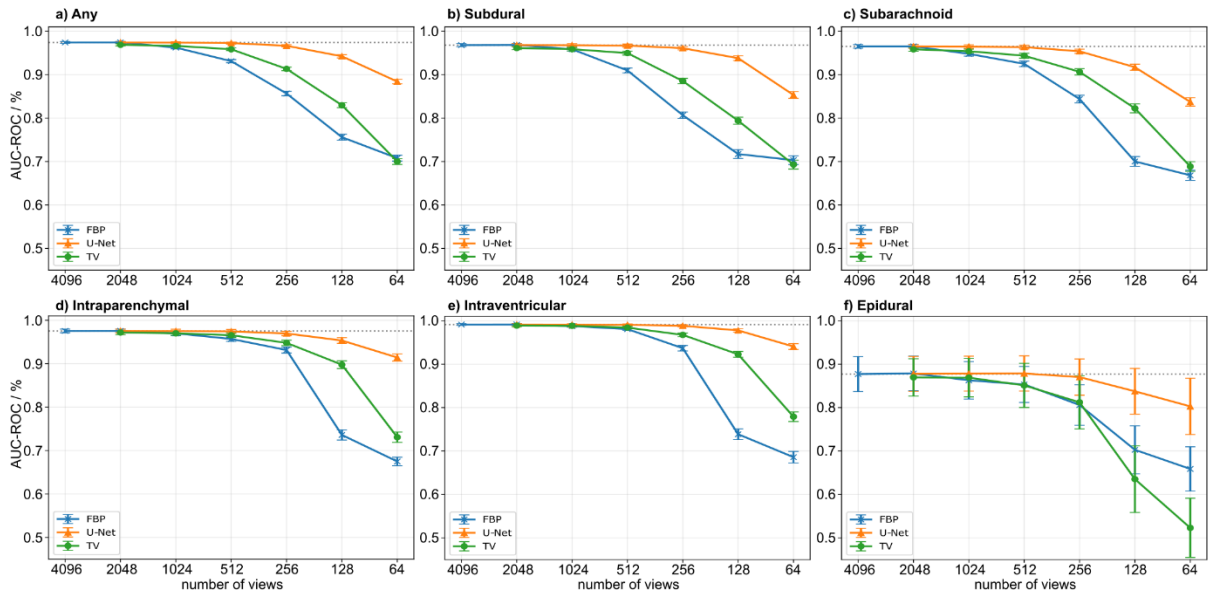


**Figure 5:** Results of the EfficientNetB2 classification network. Images a) - f) depict the mean area under the receiver operator characteristic curve (AUC-ROC) values (95% CI) associated with the any, subdural, subarachnoid, intraparenchymal, intraventricular, and epidural classes, respectively.

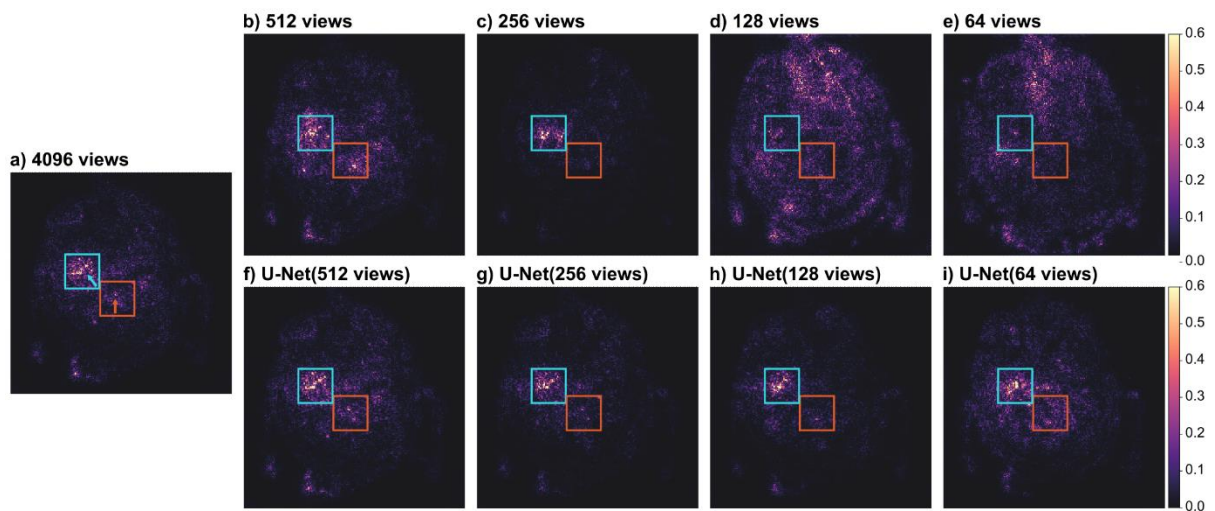


**Figure 6:** Saliency maps by the EfficientNetB2 model of the CT images of figure 3 with regards to the 'any' class. Image a) shows the saliency map of the full-view image. Images b) - e) show the saliency map of the images reconstructed from 512, 256, 128, and 64 views, respectively. Images e) - h) show the saliency maps of the images post-processed by the U-Net of the corresponding sparse-view images. All maps were normalized via min-max normalization to range [0-1]. The rectangles are at the same position as in figure 3, indicating the location of the present hemorrhages.



**Table 1**

**Structural similarity index measurement (SSIM) and peak signal-to-noise-ratio (PSNR) values of the sparse-view CT images of the RSNA test split and the CQ500 dataset.**

**The images were reconstructed by filtered backprojection (FBP) from varying number of views and then not post-processing, post-processed by the U-Net, or post-processed by the total variation-based method (TV). The data are presented as means with 95% CI in parentheses.**

**RSNA test split**

SSIM	2048 views	1024 views	512 views	256 views	128 views	64 views
FBP	1.000 (1.000-1.000)	0.994 (0.994-0.994)	0.974 (0.974-0.975)	0.906 (0.905-0.907)	0.747 (0.745-0.748)	0.574 (0.572-0.576)
U-Net	1.000 (1.000-1.000)	<b>0.999</b> <b>(0.999-0.999)</b>	<b>0.997</b> <b>(0.996-0.997)</b>	<b>0.990</b> <b>(0.990-0.990)</b>	<b>0.985</b> <b>(0.985-0.985)</b>	<b>0.960</b> <b>(0.960-0.960)</b>
TV	1.000 (1.000-1.000)	0.997 (0.996-0.997)	0.991 (0.991-0.991)	0.981 (0.981-0.981)	0.946 (0.945-0.946)	0.873 (0.872-0.873)
PSNR [dB]	2048 views	1024 views	512 views	256 views	128 views	64 views
FBP	68.102 (68.001-68.202)	54.797 (54.672-54.922)	45.268 (45.146-45.389)	35.860 (35.754-35.966)	27.631 (27.536-27.727)	20.766 (20.673-20.858)
U-Net	<b>70.490</b> <b>70.406-70.573</b>	<b>59.812</b> <b>59.723-59.901</b>	<b>52.575</b> <b>52.474-52.677</b>	<b>44.707</b> <b>(44.628-44.787)</b>	<b>41.300</b> <b>(41.249-41.352)</b>	<b>35.256</b> <b>(35.213-35.299)</b>
TV	61.986 (61.920-62.051)	53.350 (53.25-53.449)	44.323 (44.223-44.423)	36.293 (36.196-36.39)	29.464 (29.367-29.561)	23.590 (23.493-23.686)

**CQ500 dataset**

SSIM	2048 views	1024 views	512 views	256 views	128 views	64 views
FBP	1.000 (1.000-1.000)	0.987 (0.987-0.987)	0.947 (0.947-0.948)	0.814 (0.813-0.816)	0.538 (0.537-0.540)	0.314 (0.313-0.316)
U-Net	1.000 (1.000-1.000)	<b>0.999</b> <b>(0.999-0.999)</b>	<b>0.997</b> <b>(0.997-0.997)</b>	<b>0.994</b> <b>(0.994-0.995)</b>	<b>0.988</b> <b>(0.988-0.988)</b>	<b>0.972</b> <b>(0.972-0.972)</b>
TV	1.000 (1.000-1.000)	0.993 (0.993-0.993)	0.984 (0.983-0.984)	0.964 (0.963-0.964)	0.865 (0.864-0.866)	0.659 (0.657-0.660)
PSNR[dB]	2048 views	1024 views	512 views	256 views	128 views	64 views
FBP	59.744 (59.613-59.875)	44.568 (44.416-44.719)	35.416 (35.269-35.563)	27.038 (26.923-27.153)	19.577 (19.485-19.668)	12.969 (12.88-13.057)
U-Net	<b>69.795</b> <b>(69.716-69.875)</b>	<b>60.689</b> <b>(60.608-60.771)</b>	<b>54.716</b> <b>(54.627-54.804)</b>	<b>50.510</b> <b>(50.435-50.585)</b>	<b>45.210</b> <b>(45.147-45.273)</b>	<b>39.061</b> <b>(39.006-39.115)</b>
TV	56.122 (56.049-56.195)	44.772 (44.657-44.888)	35.795 (35.679-35.912)	27.975 (27.873-28.078)	21.108 (21.008-21.207)	15.199 (15.098-15.301)

**Table 2: Confusion matrices of the 'any' class of the full-view images and images of varying levels of subsampling reconstructed via filtered backprojection (FBP) from 2048 to 64 views, without post-processing (FBP) and with either U-Net post-processing or total-variation-based (TV) post-processing.**

Nr. of views		4096		2048		1024		512		256		128		64	
	actual	yes	no	yes	no	yes	no	yes	no	yes	no	yes	no	yes	no
	predicted														
FBP	yes	4,684	2,287	4,703	2,456	4,588	3,343	4,431	6,580	4,167	9,398	3,720	11,937	3,630	12,952
	no	455	31,999	436	31,830	551	30,943	708	27,706	972	24,888	1,419	22,349	1,509	21,334
U-Net	yes	X		4,686	2,293	4,659	2,104	4,673	2,388	4,568	2,541	4,344	3,277	4,025	6,287
	no			453	31,993	480	32,182	466	31,898	571	31,745	795	31,009	1,114	27,999
TV	yes	X		4,607	2,370	4,585	2,390	4,486	2,697	4,309	6,129	3,887	9,152	3,691	13,881
	no			532	31,916	554	31,896	653	31,589	830	28,157	1,252	25,134	1,448	20,405



## Supplementary Material

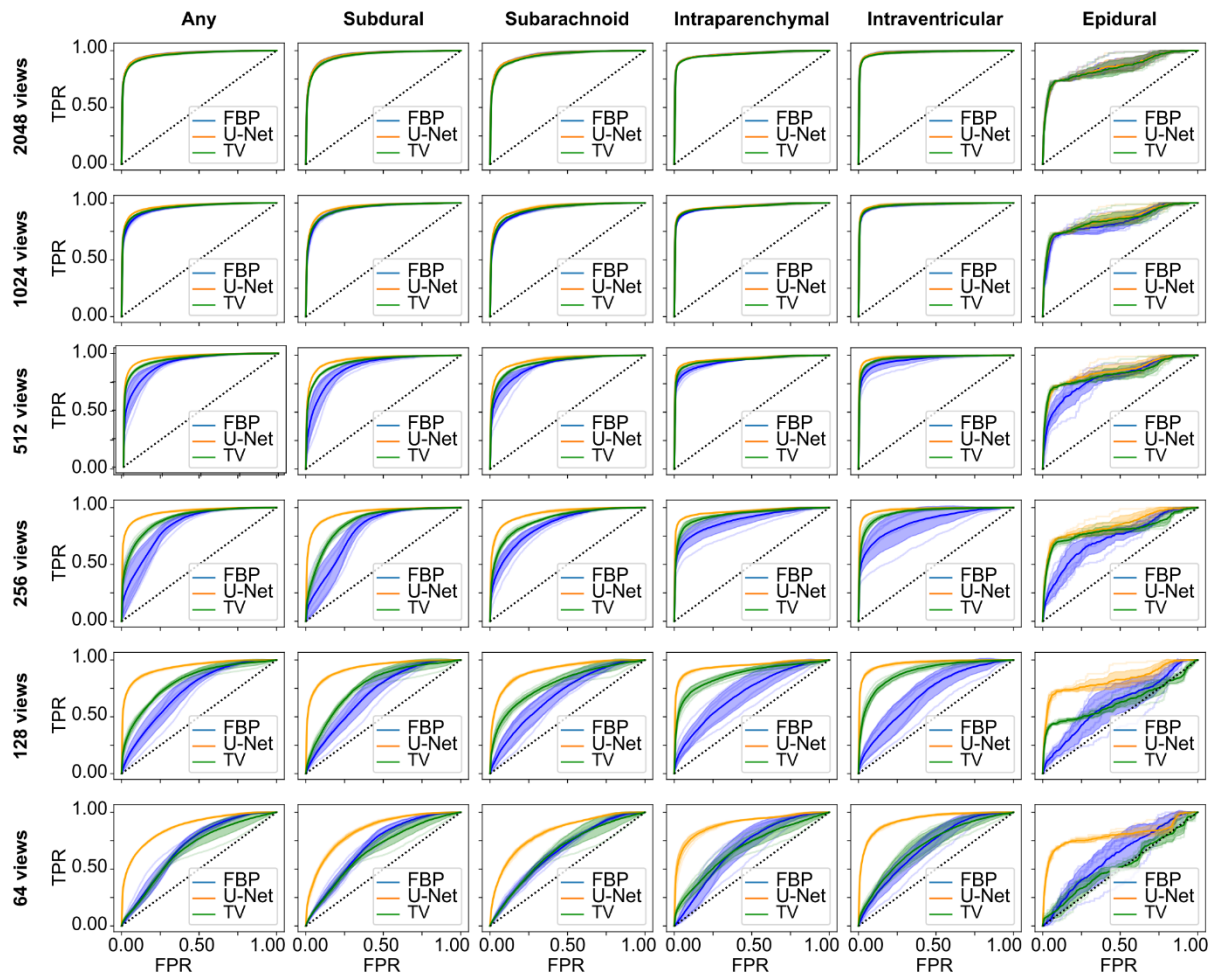


**Figure S1:** Results of the EfficientNetB2 hemorrhage classification network. Depicted are the mean receiver operator characteristic curves of the classes any, subdural, subarachnoid, intraparenchymal, intraventricular, and epidural, for the different levels of subsampling, which were used for the calculation of the individual AUC values. In addition to the results of the raw images (blue), the classification results on the images post-processed by either U-Net (orange) or the total variation-based method (green) are shown. The bold graphs are the mean curves, the colored areas mark the 95% confidence intervals.

**Table S2 Area under the receiver operator characteristics curve (AUC-ROC) values of the hemorrhage subtypes of the full-view images and images of varying levels of subsampling from 2048 to 64 views, without post-processing (FBP) and with either TV post-processing or U-Net post-processing with 95% confidence intervals in brackets.**

subtype	Nr. of views	4096	2048	1024	512	256	128	64
any	FBP	0.974 (0.972-0.976)	0.974 (0.972-0.976)	0.962 (0.960-0.965)	0.931 (0.928-0.935)	0.857 (0.852-0.862)	0.756 (0.749-0.763)	0.708 (0.701-0.714)
	U-Net	x	0.974 (0.972-0.976)	<b>0.974</b> <b>(0.972-0.976)</b>	<b>0.973</b> <b>(0.971-0.975)</b>	<b>0.967</b> <b>(0.964-0.969)</b>	<b>0.942</b> <b>(0.939-0.946)</b>	<b>0.884</b> <b>(0.879-0.889)</b>
	TV	x	0.969 (0.966-0.971)	0.966 (0.964-0.969)	0.958 (0.955-0.961)	0.913 (0.909-0.917)	0.830 (0.824-0.835)	0.700 (0.693-0.707)
subdural	FBP	0.968 (0.965-0.972)	0.968 (0.965-0.972)	0.958 (0.954-0.962)	0.910 (0.904-0.915)	0.807 (0.799-0.814)	0.717 (0.707-0.727)	0.703 (0.693-0.713)
	U-Net	x	0.968 (0.965-0.972)	<b>0.968</b> <b>(0.964-0.971)</b>	<b>0.967</b> <b>(0.963-0.970)</b>	<b>0.961</b> <b>(0.957-0.965)</b>	<b>0.938</b> <b>(0.933-0.943)</b>	<b>0.853</b> <b>(0.845-0.861)</b>
	TV	x	0.961 (0.957-0.965)	0.959 (0.955-0.963)	0.950 (0.945-0.954)	0.885 (0.879-0.891)	0.794 (0.786-0.802)	0.693 (0.683-0.703)
subarachnoid	FBP	0.965 (0.961-0.969)	0.965 (0.961-0.969)	0.948 (0.943-0.953)	0.925 (0.919-0.931)	0.844 (0.835-0.853)	0.700 (0.689-0.711)	0.668 (0.657-0.680)
	U-Net	x	0.965 (0.961-0.969)	<b>0.965</b> <b>(0.961-0.969)</b>	<b>0.963</b> <b>(0.959-0.968)</b>	<b>0.954</b> <b>(0.949-0.959)</b>	<b>0.917</b> <b>(0.910-0.924)</b>	<b>0.837</b> <b>(0.827-0.847)</b>
	TV	x	0.958 (0.954-0.963)	0.954 (0.949-0.959)	0.944 (0.938-0.949)	0.907 (0.899-0.914)	0.822 (0.812-0.833)	0.689 (0.677-0.700)
intraparenchymal	FBP	0.976 (0.971-0.980)	0.976 (0.971-0.980)	0.970 (0.965-0.975)	0.957 (0.951-0.963)	0.931 (0.925-0.938)	0.736 (0.724-0.748)	0.675 (0.665-0.685)
	U-Net	x	0.976 (0.971-0.980)	<b>0.975</b> <b>(0.971-0.979)</b>	<b>0.974</b> <b>(0.970-0.979)</b>	<b>0.970</b> <b>(0.965-0.974)</b>	<b>0.953</b> <b>(0.947-0.960)</b>	<b>0.914</b> <b>(0.906-0.922)</b>
	TV	x	0.972 (0.967-0.977)	0.970 (0.965-0.975)	0.966 (0.960-0.971)	0.948 (0.942-0.954)	0.898 (0.889-0.907)	0.731 (0.719-0.743)
intraventricular	FBP	0.991 (0.989-0.993)	0.991 (0.989-0.993)	0.988 (0.985-0.990)	0.981 (0.978-0.984)	0.937 (0.930-0.943)	0.739 (0.726-0.751)	0.686 (0.673-0.699)
	U-Net	x	0.991 (0.989-0.993)	<b>0.991</b> <b>(0.989-0.993)</b>	<b>0.991</b> <b>(0.988-0.993)</b>	<b>0.988</b> <b>(0.986-0.991)</b>	<b>0.978</b> <b>(0.974-0.981)</b>	<b>0.941</b> <b>(0.934-0.947)</b>
	TV	x	0.989 (0.987-0.991)	0.988 (0.986-0.991)	0.984 (0.981-0.987)	0.967 (0.963-0.972)	0.923 (0.916-0.929)	0.779 (0.768-0.790)
epidural	FBP	0.877 (0.837-0.918)	<b>0.879</b> <b>(0.839-0.918)</b>	0.863 (0.820-0.906)	0.853 (0.812-0.895)	0.806 (0.759-0.852)	0.703 (0.647-0.758)	0.659 (0.608-0.710)
	U-Net	x	0.878 (0.837-0.918)	<b>0.878</b> <b>(0.838-0.918)</b>	<b>0.879</b> <b>(0.838-0.919)</b>	<b>0.870</b> <b>(0.828-0.912)</b>	<b>0.837</b> <b>(0.785-0.890)</b>	<b>0.803</b> <b>(0.738-0.868)</b>
	TV	x	0.869 (0.827-0.912)	0.869 (0.825-0.913)	0.851 (0.800-0.902)	0.812 (0.751-0.873)	0.635 (0.558-0.712)	0.523 (0.455-0.591)

**Table S3 Confusion matrices of the hemorrhage subtypes of the full-view images and images of varying levels of subsampling from 2048 to 64 views, without post-processing (FBP) and with either TV post-processing or U-Net post-processing**

Nr. of views			4096		2048		1024		512		256		128		64	
subtype	type	actual	yes	no	yes	no	yes	no	yes	no	yes	no	yes	no	yes	no
		predicted														
any	FBP	yes	4684	2287	4703	2456	4588	3343	4431	6580	4167	9398	3720	11937	3630	12952
		no	455	31999	436	31830	551	30943	708	27706	972	24888	1419	22349	1509	21334
	U-Net	yes			4686	2293	4659	2104	4673	2388	4568	2541	4344	3277	4025	6287
		no			453	31993	480	32182	466	31898	571	31745	795	31009	1114	27999
	TV	yes			4607	2370	4585	2390	4486	2697	4309	6129	3887	9152	3691	13881
		no			532	31916	554	31896	653	31589	830	28157	1252	25134	1448	20405
subdural	FBP	yes	1994	3185	2003	3369	1998	4364	1933	8634	1912	14489	1489	13628	1448	13502
		no	209	34037	200	33853	205	32858	270	28588	291	22733	714	23594	755	23720
	U-Net	yes			1984	2988	1997	3252	1990	3294	1949	3453	1884	4632	1704	8466
		no			219	34234	206	33970	213	33928	254	33769	319	32590	499	28756
	TV	yes			1925	2848	1906	2926	1937	4339	1872	8718	1781	13284	1449	13604
		no			278	34374	297	34296	266	32883	331	28504	422	23938	754	23618
subarachnoid	FBP	yes	1578	2612	1588	2888	1537	3995	1405	3885	1324	8761	1159	13452	1094	14489
		no	204	35031	194	34755	245	33648	377	33758	458	28882	623	24191	688	23154
	U-Net	yes			1588	2812	1586	2809	1583	2848	1537	3182	1464	4857	1338	8247
		no			194	34831	196	34834	199	34795	245	34461	318	32786	444	29396
	TV	yes			1549	2812	1532	2973	1533	4043	1431	5357	1288	9354	1154	14011
		no			233	34831	250	34670	249	33600	351	32286	494	28289	628	23632
intraparenchymal	FBP	yes	1637	1527	1636	1529	1622	1770	1542	2004	1460	3659	1171	12579	1272	16257
		no	149	36112	150	36110	164	35869	244	35635	326	33980	615	25060	514	21382
	U-Net	yes			1639	1551	1636	1553	1619	1207	1606	1428	1589	2666	1499	5471
		no			147	36088	150	36086	167	36432	180	36211	197	34973	287	32168
	TV	yes			1609	1213	1616	1423	1611	1921	1542	2384	1387	3790	1183	12355
		no			177	36426	170	36216	175	35718	244	35255	399	33849	603	25284
intraventricular	FBP	yes	1143	1244	1145	1316	1135	1815	1121	2978	1044	6526	817	14000	791	15983
		no	59	36979	57	36907	67	36408	81	35245	158	31697	385	24223	411	22240
	U-Net	yes			1145	1335	1144	1328	1145	1356	1123	1195	1103	2475	1055	5061
		no			57	36888	58	36895	57	36867	79	37028	99	35748	147	33162
	TV	yes			1130	1158	1132	1447	1130	2124	1077	3059	1026	6534	889	11824
		no			72	37065	70	36776	72	36099	125	35164	176	31689	313	26399
epidural	FBP	yes	66	2148	66	2149	66	2703	63	4336	66	9040	61	12805	56	14648
		no	25	37186	25	37185	25	36631	28	34998	25	30294	30	26529	35	24686
	U-Net	yes			66	2134	66	2161	66	2359	66	2831	65	2521	65	4378
		no			25	37200	25	37173	25	36975	25	36503	26	36813	26	34956
	TV	yes			66	1912	66	1815	66	2173	64	3245	41	3255	42	12137
		no			25	37422	25	37519	25	37161	27	36089	50	36079	49	27197